Three-dimensional Finite Element Analysis of Tunnels and Foundations

A.E. Groen
Department of Civil Engineering, Delft University of Technology
P.O. Box 5048, 2600 GA Delft, The Netherlands

R. de Borst
Department of Civil Engineering, Delft University of Technology
P.O. Box 5048, 2600 GA Delft, The Netherlands

An increasing need for underground infrastructure in The Netherlands requires knowledge about the behavior of construction in soft soils. In this contribution, attention is focused on three-dimensional numerical simulation of construction works in soils, i.e. tunneling and foundations. In order to perform such simulations, robust numerical tools are a first requirement. The development of such numerical tools will be presented, as well as some typical three-dimensional test cases such as a guided pipe-jacking and the leaning tower of Pisa.

Key words: **finite element method, element locking, clay, sand, soil mechanics**

1 Introduction

The density of infrastructure is increasing dramatically almost everywhere in the world. This results in construction works close to, or under already existing infrastructure. Obviously, damage to already existing infrastructure needs to be avoided or kept to a minimum.
It is therefore of vital importance that knowledge is obtained about the strength and deformation behavior of the surrounding soil. In contrast to most engineering materials in which adjustment of mechanical properties and structural optimization lead to an optimal design, soil is hardly susceptible to improvement of mechanical properties. At best, it is an extremely costly process. Furthermore, areas of economic interest such as estuaries mostly contain soils which can be characterized as extremely weak.
In the past decades, the finite element method has undoubtedly become the most popular tool for the analysis of the strength and deformation behavior of structures. Due to the advent of powerful computational hardware it has now become possible to combine realistic material descriptions for soils with three-dimensional finite element analysis. However, several difficulties still exist.
The most obvious is the finite element modeling itself, i.e. a proper description of the geometry and boundary conditions which both may change during the calculation process. Furthermore, the interpretation and visualization of results can be difficult especially in a three-dimensional configuration. In addition, three-dimensional finite element analysis puts stronger requirements on the

HERON, Vol. 42, No. 4 (1997) ISSN 0046-7316

stability of the numerical processes. Both the spatial discretization (the finite elements) and the material description pose difficulties which mainly originate from a three-dimensional state of stress and strain. Finally, three-dimensional analysis puts a strong requirement on hardware and also on the experience of the user.

This study focuses on the nonlinear analysis of the strength and deformation behavior of soil bodies. Firstly, the development of eight-noded brick elements which are able to simulate volume preserving and dilatant/contractant soil behavior will be shown. The issue of element locking will be addressed and it will be shown that common solutions like the $\bar{B}$-bar approach (Hughes 1980) are unable to simulate dilatant/contractant soil behavior. Furthermore, stability of the developed elements will be addressed and their properties are demonstrated in elementary tests and in the analysis of a square footing. Secondly, the Modified Cam-Clay model will be discussed and utilized to simulate the construction of a guided pipe-jacking. Thirdly, a double-hardening model for the behavior of sand will be presented. This model will be utilized for the simulation of the leaning tower of Pisa. Both for the guided pipe-jacking and the leaning tower of Pisa emphasis is placed on the performance of the developed elements.

1.1 *A note on stress and strain definitions*

For convenience in a finite element environment, the stress tensor $\boldsymbol{\sigma}$ and the strain tensor $\boldsymbol{\varepsilon}$ are introduced in a vector format as

$$\boldsymbol{\sigma} = [\sigma_{xx},\sigma_{yy},\sigma_{zz},\sigma_{xy},\sigma_{yz},\sigma_{zx}]^T \tag{1}$$

$$\boldsymbol{\varepsilon} = [\varepsilon_{xx},\varepsilon_{yy},\varepsilon_{zz},2\varepsilon_{xy},2\varepsilon_{yz},2\varepsilon_{zx}]^T \tag{2}$$

in which the engineering shear strains have been utilized instead of the tensorial shear strains. The hydrostatic pressure and the volumetric strain are defined as

$$p = \tfrac{1}{3}(\sigma_{xx} + \sigma_{yy} + \sigma_{zz}) \tag{3}$$

$$\varepsilon_v = \varepsilon_{xx} + \varepsilon_{yy} + \varepsilon_{zz} \tag{4}$$

in which "p" is the hydrostatic tensile component and ε_v is the dilatancy. Upon introduction of the projection vector $\boldsymbol{\pi} = [1\,,1\,,1\,,0\,,0\,,0]^T$ one can define the deviatoric stresses and strains,

$$\boldsymbol{\xi} = \boldsymbol{\sigma} - p\boldsymbol{\pi} \tag{5}$$

$$\boldsymbol{\gamma} = \boldsymbol{\varepsilon} - \tfrac{1}{3}\varepsilon_v\boldsymbol{\pi} \tag{6}$$

The effective deviatoric stress is defined according to

$$q = \sqrt{\tfrac{3}{2}\boldsymbol{\xi}^T R\boldsymbol{\xi}}\ ;\ R = \mathrm{diag}[1,1,1,2,2,2] \tag{7}$$

The Lode angle θ is defined as

$$\cos 3\theta = -\frac{27}{2}\frac{J_3}{q^3}\ ;\ J_3 = \xi_{xx}\xi_{yy}\xi_{zz} + \xi_{xy}\xi_{yz}\xi_{zx} - 2(\xi_{xx}\xi_{yz}^2 + \xi_{yy}\xi_{zx}^2 + \xi_{zz}\xi_{xy}^2) \tag{8}$$

2 Volumetric locking

A phenomenon frequently encountered in finite element analysis of mass structures is so-called "volumetric locking". This can be conceived as the inability of a discretized system to represent the deformations of the underlying continuum imposed by the loading, the boundary conditions and by the constitutive model. To state the problem in simple terms, we refer to the elementary element patch of Figure 1. For simplicity we have selected simple, constant strain triangles and we have adopted a plane-strain configuration, so that the out-of-plane strains are zero. Obviously, any constitutive relation that makes the material incompressible, such as incompressible elasticity, or Mises-Huber plasticity at fully developed plastic flow, constrains the movement of the right-upper node to a horizontal line when applying this kinematic constraint to the right-lower element. Similarly, the left-upper element constrains the possible displacement of this node to a vertical line, as also indicated in Figure 1. Evidently, no displacements of the node are possible. This observation is still valid when a large element patch is considered (cf. Hughes 1987). In that case, the deformations of each element are restrained by the boundary conditions imposed by their neighboring elements. The result is that an excessively overstiff behavior is obtained in incompressible elasticity while a severe overestimation of the collapse load is observed in elasto-plastic calculations, if a proper limit load can be obtained at all. This phenomenon, which occurs particularly for low-order finite elements in plane-strain, axisymmetric and three-dimensional configurations, is now well-known in the literature and an abundance of possible solutions have been put forward. One of the early solutions is the use of special arrangements of elements, such as the crossed triangular patches (Nagtegaal *et al.* 1974), the use of reduced or selective integration (Zienkiewicz and Taylor 1989), which is closely related to the $\bar{B}$-bar approach of Hughes (1980), the independent interpolation of displacements and pressures (Sussmann and Bathe 1987, Van den Bogert *et al.* 1991), where the pressure degrees-of-freedom are usually condensed at element level, the mixed approaches, where especially the Enhanced Assumed Strain concept of Simo and his co-workers has gained much popularity, and finally the use of higher-order displacement models (Sloan and Randolph 1982, de Borst 1982), which is maybe the "royal road", an expensive, but very robust solution.

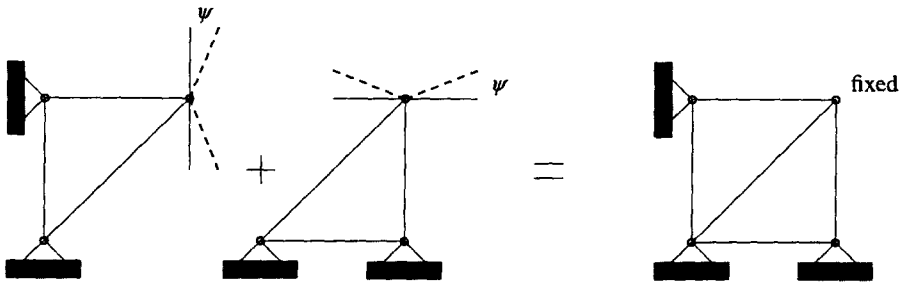

Fig. 1. Locking of two three-nodel triangular elements for fully developed plastic flow.

While the phenomenon of "element locking" in isochoric deformations has received much attention in the past, it has not been recognized at a large scale that dilatant or contractant plastic flow imposes essentially the same kinematic constraint upon the elements. As will be argued below in a

more rigorous manner, plastic dilatancy or contraction essentially imposes a pointwise relation between the shear deformation and the volumetric deformation. For the constant strain elements of Figure 1 this means that if the right-lower element is sheared, a volumetric strain *must* occur, and the node can only translate along one of the dashed lines emanating from the node, where the amount of uplift is governed by the angle of dilatancy ψ. Similarly, any shearing applied to the other element also causes volumetric straining, and as a result the movements of the same node are restricted to the other set of dashed lines. The conclusion is that, similar to the case of isochoric deformations, which obviously is just a special case ($\psi = 0$), no movement is allowed and no proper collapse load can be obtained for ideal plasticity.

Because of the observed locking behavior in low-order elements, numerous improvements of such elements by mixed methods have been put forward. Due to the strain-driven character of the integration algorithms that arise from plasticity models, it is convenient to restrict the application of mixed methods to so-called "assumed strain elements" in which the strain rate is interpolated independently from the velocity. Examples of "assumed strain elements" are the *B*-bar method (Hughes 1980) and the incompatible modes element (Wilson *et al.* 1971, Taylor *et al.* 1976). Recently, Simo and Rifai (1990) have proposed the so-called "Enhanced Assumed Strain concept". Herein, the strain rates are assumed to be an additive decomposition of the strain rates following from compatibility and an additional strain rate field.

2.1 *The kinematic constraint imposed by dilatant/contractant plasticity*

As has been argued before, dilatant/contractant (and volume preserving) plastic flow imposes a constraint upon the velocity field of a finite element. This is demonstrated by one of the most frequently used yield criteria for soils and rocks, the over two centuries-old Coulomb criterion. Expressed in terms of principal stresses, the Mohr-Coulomb yield function reads:

$$f = \tfrac{1}{2}(\sigma_3 - \sigma_1) + \tfrac{1}{2}(\sigma_3 + \sigma_1)\sin\phi - c\cos\phi \tag{9}$$

with ϕ the angle of internal friction and c the cohesion of the material. A typical feature of the Mohr-Coulomb criterion is that the intermediate principal stress σ_2, $\sigma_1 \leq \sigma_2 \leq \sigma_3$, does not enter the yield function. For an associative flow rule, where the plastic strain rate $\dot{\varepsilon}^P$ is derived by differentiating the yield function f with respect to the stress tensor $\boldsymbol{\sigma}$, $\dot{\boldsymbol{\varepsilon}}^P = \dot{\lambda}\partial f/\partial\boldsymbol{\sigma}$, with $\dot{\lambda}$ a proportionality factor, the above observation implies that there is no plastic straining in the direction of the intermediate principal stress. This property is preserved if a non-associative flow rule is employed, such that the plastic strain rate is obtained by assuming

$$\dot{\boldsymbol{\varepsilon}}^P = \dot{\lambda}\frac{\partial g}{\partial \boldsymbol{\sigma}} \tag{10}$$

with g a plastic potential function that resembles the yield function f:

$$g = \tfrac{1}{2}(\sigma_3 - \sigma_1) + \tfrac{1}{2}(\sigma_3 + \sigma_1)\sin\psi - \text{constant} \tag{11}$$

with ψ an additional material constant, which is commonly named the angle of dilatancy. Experiments show that the dilatancy angle ψ is usually significantly smaller than the angle of internal friction ϕ ($\psi < \phi$). For cohesionless materials, e.g., dry sands, this is a requirement that follows from thermodynamical considerations (Vermeer and de Borst 1984). The angle of dilatancy controls the amount of plastic volume change. Defining the volumetric plastic strain rate as

$$\dot{\varepsilon}_v^p = \dot{\varepsilon}_1^p + \dot{\varepsilon}_2^p + \dot{\varepsilon}_3^p \tag{12}$$

and introducing the rate of plastic shear deformation

$$\dot{\gamma}^p = \dot{\varepsilon}_3^p - \dot{\varepsilon}_1^p \tag{13}$$

one can use eqs. (10) and (11) to derive that

$$\dot{\varepsilon}_v^p = \dot{\gamma}^p \sin\psi \tag{14}$$

which shows that the angle of dilatancy ψ sets the ratio between the rate of plastic shear deformation and the rate of plastic volume change. For $\psi > 0$ an irreversible increase of volume occurs, while for $\psi < 0$ a decrease is predicted (plastic contraction). $\psi = 0$ is the special case of plastically volume-preserving (isochoric) flow. The Tresca plasticity model with an associative flow rule is obtained by setting $\phi = \psi = 0$ in eqs. (9) and (11). This yield criterion is often employed to characterize the mechanical behavior of metals and clays under undrained conditions.
At collapse, the magnitude of the elastic strain rate is negligible with respect to the magnitude of the plastic strain rate. Hence, relation (14) carries over to the total strain rate and subsequently changes into

$$\dot{\varepsilon}_v = \dot{\gamma}\sin\psi \tag{15}$$

which effectively imposes a kinematic constraint on the possible velocity field. It is emphasised that this constraint condition applies irrespective of the value of ψ, and that $\psi = 0$ (volume-preserving plastic flow) is just a special case.
In computations, the Mohr-Coulomb and Tresca yield criteria pose some problems because of the corners in the yield surface, which may deteriorate convergence of the Newton-Raphson procedure at global level. Improper handling of the constitutive relation should not obscure the issue of element locking and especially lack of robustness of the element formulation. Therefore, in the forthcoming computations the Mohr-Coulomb and Tresca yield functions are approximated by the smooth Drucker-Prager and Von Mises yield functions

$$f = q + \alpha p - k \tag{16}$$

with "p" the first invariant of the stress tensor and "q" the effective deviatoric stress. In the calculations presented the material parameters α and k are related to the angle of internal friction ϕ and the cohesion c via

$$\alpha = \frac{6\sin\phi}{3-\sin\phi} \qquad \text{and} \qquad k = \frac{6c\cos\phi}{3-\sin\phi} \tag{17}$$

The Von Mises yield function is obtained for $\phi = 0$, so that $\alpha = 0$ and $k = 2c$. As with the Mohr-Coulomb yield function a non-associative flow rule can be obtained, but now with "g" defined as

$$g = q + \beta p - \text{constant} \tag{18}$$

and β a dilatancy factor which can be related to the angle of dilatacy ψ in a fashion similar to that between α and the angle of internal friction ϕ.

2.2 *Locking for eight-noded brick elements*

We choose the principal axes of the strain rate tensor to coincide with the local ξ, η, ζ-coordinate system of an element. For the Mohr-Coulomb yield function resembling plastic potential (11), eq. (15) specializes as

$$(1-\sin\psi)\dot{\varepsilon}_\xi + (1+\sin\psi)\dot{\varepsilon}_\eta + \dot{\varepsilon}_\zeta = 0 \tag{19}$$

for any cyclic permutation ξ, η, ζ. Note that in this formulation only the normal strain rates are involved. This is a direct consequence of a coinciding isoparametric and principal space combined with the assumption of a Mohr-Coulomb plasticity model.

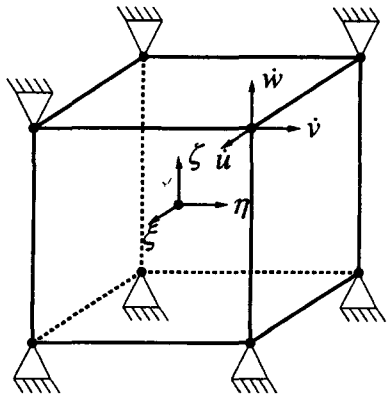

Fig. 2. Three-dimensional eight-noded brick with all nodes restrained except one.

We now consider an eight-noded brick element with all nodes restrained except one, Figure 2. The compatible velocities are interpolated in a standard isoparametric fashion as

$$\begin{aligned} \dot{u}(\xi,\eta,\zeta) &= \tfrac{1}{8}(1+\xi)(1+\eta)(1+\zeta)\dot{u} \\ \dot{v}(\xi,\eta,\zeta) &= \tfrac{1}{8}(1+\xi)(1+\eta)(1+\zeta)\dot{v} \\ \dot{w}(\xi,\eta,\zeta) &= \tfrac{1}{8}(1+\xi)(1+\eta)(1+\zeta)\dot{w} \end{aligned} \tag{20}$$

in which $\dot{u}, \dot{v}, \dot{w}$ are the nodal velocities. The normal strain rates are obtained by differentiation of the velocities with respect to the isoparametric coordinates.

$$\begin{bmatrix} \dot{\varepsilon}_x \\ \dot{\varepsilon}_y \\ \dot{\varepsilon}_z \end{bmatrix} = \tfrac{1}{8}\begin{bmatrix} 1+\eta+\zeta+\eta\zeta & 0 & 0 \\ 0 & 1+\xi+\zeta+\xi\zeta & 0 \\ 0 & 0 & 1+\xi+\eta+\xi\eta \end{bmatrix}\begin{bmatrix} \dot{u} \\ \dot{v} \\ \dot{w} \end{bmatrix} \tag{21}$$

Eq. (21) can be written in a more compact form as

$$\dot{\boldsymbol{\varepsilon}} = \boldsymbol{B}\dot{\boldsymbol{u}} \tag{22}$$

in which $\dot{\boldsymbol{\varepsilon}} = [\dot{\varepsilon}_x, \dot{\varepsilon}_y, \dot{\varepsilon}_z]$, $\boldsymbol{u} = [\dot{u}, \dot{v}, \dot{w}]$ and

$$\boldsymbol{B} = \tfrac{1}{8}\begin{bmatrix} 1+\eta+\zeta+\eta\zeta & 0 & 0 \\ 0 & 1+\xi+\zeta+\xi\zeta & 0 \\ 0 & 0 & 1+\xi+\eta+\xi\eta \end{bmatrix} \tag{23}$$

Substitution of eq. (21) into the kinematic constraint (19) gives, after ordering the terms with coefficients *constant*, $\xi, \eta, \zeta, \xi\eta, \xi\zeta, \eta\zeta$

$(1-\sin\psi)\dot{u} + (1+\sin\psi)\dot{v} + \dot{w} = 0$ (constant term)

$$\begin{aligned} (\xi): &\quad (1+\sin\psi)\dot{v} + \dot{w} = 0 \\ (\eta): &\quad (1-\sin\psi)\dot{u} + \dot{w} = 0 \\ (\zeta): &\quad (1-\sin\psi)\dot{u} + (1+\sin\psi)\dot{v} = 0 \\ (\xi\eta): &\quad \dot{w} = 0 \\ (\eta\zeta): &\quad (1+\sin\psi)\dot{v} = 0 \\ (\zeta\xi): &\quad (1-\sin\psi)\dot{u} = 0 \end{aligned} \tag{24}$$

Obviously, the only possible solution is $(\dot{u}, \dot{v}, \dot{w}) = 0$. In other words, the elements locks in volume-preserving and in dilatant flow.

As a possible solution we consider the *B*-bar element (Hughes 1980). This element is locking-free under volume-preserving conditions. Formulation of this element only requires a modification of eq. (22)

$$\dot{\boldsymbol{\varepsilon}} = \bar{\boldsymbol{B}}\dot{\boldsymbol{u}} \tag{25}$$

and is therefore easy to implement in a general-purpose finite element code. For the element shown in Figure 2 this leads to the following form for the normal strain rates

$$\begin{bmatrix} \dot{\varepsilon}_x \\ \dot{\varepsilon}_y \\ \dot{\varepsilon}_z \end{bmatrix} = \bar{\boldsymbol{B}}\dot{\boldsymbol{u}} = \frac{1}{8}\begin{bmatrix} 1+\frac{2}{3}(\eta+\zeta+\eta\zeta) & -\frac{1}{3}(\xi+\zeta+\xi\zeta) & -\frac{1}{3}(\xi+\eta+\xi\eta) \\ -\frac{1}{3}(\eta+\zeta+\eta\zeta) & 1+\frac{2}{3}(\xi+\zeta+\xi\zeta) & -\frac{1}{3}(\xi+\eta+\xi\eta) \\ -\frac{1}{3}(\eta+\zeta+\eta\zeta) & -\frac{1}{3}(\xi+\zeta+\xi\zeta) & 1+\frac{2}{3}(\xi+\eta+\xi\eta) \end{bmatrix}\begin{bmatrix} \dot{u} \\ \dot{v} \\ \dot{w} \end{bmatrix} \tag{26}$$

Substitution into the kinematic constraint (19) gives, after ordering the terms with coefficients *constant*, ξ, η, ζ, $\xi\eta$, $\xi\zeta$, $\eta\zeta$

$$(1-\sin\psi)\dot{u} + (1+\sin\psi)\dot{v} + \dot{w} = 0 \text{ (constant term)}$$

$$\begin{aligned} (\xi)&: \quad \sin\psi\dot{v} = 0 \\ (\eta)&: \quad -\sin\psi\dot{u} = 0 \\ (\zeta)&: \quad -\sin\psi\dot{u} + \sin\psi\dot{v} = 0 \\ (\xi\eta)&: \quad -\tfrac{1}{3}(1-\sin\psi)\dot{u} - \tfrac{1}{3}(1+\sin\psi)\dot{v} + \tfrac{2}{3}\dot{w} = 0 \\ (\eta\zeta)&: \quad -\tfrac{1}{3}(1-\sin\psi)\dot{u} + \tfrac{2}{3}(1+\sin\psi)\dot{v} - \tfrac{1}{3}\dot{w} = 0 \\ (\zeta\xi)&: \quad +\tfrac{2}{3}(1-\sin\psi)\dot{u} - \tfrac{1}{3}(1+\sin\psi)\dot{v} - \tfrac{1}{3}\dot{w} = 0 \end{aligned} \tag{27}$$

which reveals that the $\bar{B}$-bar element is not able to accommodate the kinematic constraint (19) for $(\dot{u}, \dot{v}, \dot{w}) \neq (0, 0, 0)$ when $\psi \neq 0$. Hence, locking is expected in dilatant flow. However, it can be observed from (27) that the $\bar{B}$-bar element is indeed locking-free for $\psi = 0$.

2.3 *Elements with enhanced strain fields*

Obviously, the application of the $\bar{B}$-bar element does not solve the problem of element locking in dilatant plastic flow. The kinematic constraint (19) which is imposed on the element configuration entails (a): the definition of the shear strain γ which is generally dependent on the material model and (b): an angle of dilatancy which is dependent on the material model and in most cases not constant. A $\bar{B}$-bar method for a non-locking element in dilatant plastic flow would therefore require the material model to be incorporated into the definition of the strain-displacement relation. This would destroy the modular structure of a general purpose finite element code and is therefore not an elegant solution.

A possible solution would be to incorporate incompatible fields into the definition of the strain rates. This method has been proposed by Simo and Rifai (1990) and is referred to as the "Enhanced Assumed Strain concept". The key point of this method is relaxation of the compatibility conditions. As a result, the strain rates $\dot{\boldsymbol{\varepsilon}}$ are discretized as

$$\dot{\boldsymbol{\varepsilon}} = \boldsymbol{B}\dot{\boldsymbol{a}} + \boldsymbol{M}\dot{\boldsymbol{\alpha}} \tag{28}$$

in which $\dot{\boldsymbol{a}}$ are the nodal velocities, $\boldsymbol{B}$ is the standard isoparametric discrete strain-displacement operator, $\dot{\boldsymbol{\alpha}}$ are the additional strain rate variables and $\boldsymbol{M}$ contains the shape functions for the additional strain rate variables. In order to ensure satisfaction of the patch test (Taylor *et al.* 1986), $\boldsymbol{M}$ has to meet the requirement

$$\int_V M \; dV = 0 \tag{29}$$

Two other conditions which have to be satisfied when constructing the additional strain rate interpolations (Simo and Rifai 1990) are: (i) the additional strain rate interpolations should be linearly independent, and (ii) the additional strain rates have to be linearly independent from the compatible strain rates.

The element stiffness matrix also includes the additional strain rate variables and is given by

$$\begin{bmatrix} K & \Gamma \\ \Upsilon & Q \end{bmatrix} \begin{bmatrix} \dot{a} \\ \dot{\alpha} \end{bmatrix} = \begin{bmatrix} f_a \\ f_\alpha \end{bmatrix} \tag{30}$$

Because the strain rate variables $\dot{\alpha}$ do not have to be continuous across interelement boundaries, they can be eliminated at element level so that only the compatible velocities $\dot{a}$ are present in the global system of equations. The condensed system now attains the following format:

$$\left[K - \Gamma Q^{-1} \Upsilon\right] \dot{a} = f_a - \Gamma Q^{-1} f_a \tag{31}$$

A rational way to formulate non-locking elements via the Enhanced Assumed Strain method is to "enhance" each non-constant term in the deformation constraint resulting from a standard isoparametric eight-noded brick element c.f. eq. (24) with one additional degree-of-freedom

$$\begin{array}{lll} (\xi): & (1+\sin\psi)\dot{v} + \dot{w} = 0 & +\dot{\alpha}_1 \\ (\eta): & (1-\sin\psi)\dot{u} + \dot{w} = 0 & +\dot{\alpha}_2 \\ (\zeta): & (1-\sin\psi)\dot{u} + (1+\sin\psi)\dot{v} = 0 & +\dot{\alpha}_3 \\ (\xi\eta): & \dot{w} = 0 & +\dot{\alpha}_4 \\ (\eta\zeta): & (1+\sin\psi)\dot{v} = 0 & +\dot{\alpha}_5 \\ (\zeta\xi): & (1-\sin\psi)\dot{u} = 0 & +\dot{\alpha}_6 \end{array} \tag{32}$$

The following "enhancements" to the normal strain rates of the element in Figure 2 have been considered:

$$\begin{bmatrix} \dot{\varepsilon}_x \\ \dot{\varepsilon}_y \\ \dot{\varepsilon}_z \end{bmatrix} = B\dot{u} + M\dot{\alpha} = \frac{1}{8} \begin{bmatrix} 1+\eta+\zeta+\eta\zeta & 0 & 0 \\ 0 & 1+\xi+\zeta+\xi\zeta & 0 \\ 0 & 0 & 1+\xi+\eta+\xi\eta \end{bmatrix} \begin{bmatrix} \dot{u} \\ \dot{v} \\ \dot{w} \end{bmatrix} + \tag{33a}$$

$$\begin{bmatrix} \xi & 0 & 0 \\ 0 & \eta & 0 \\ 0 & 0 & \zeta \end{bmatrix} \begin{bmatrix} \dot{\alpha}_1 \\ \dot{\alpha}_2 \\ \dot{\alpha}_3 \end{bmatrix} + \begin{bmatrix} \xi(\eta+\zeta) & 0 & 0 \\ 0 & \eta(\xi+\zeta) & 0 \\ 0 & 0 & \zeta(\xi+\eta) \end{bmatrix} \begin{bmatrix} \dot{\alpha}_4 \\ \dot{\alpha}_5 \\ \dot{\alpha}_6 \end{bmatrix}$$

The resulting element will be referred to as the EAS 6(a) element.

$$\begin{bmatrix}\dot{\varepsilon}_x\\ \dot{\varepsilon}_y\\ \dot{\varepsilon}_z\end{bmatrix} = \boldsymbol{B}\dot{\boldsymbol{u}} + \boldsymbol{M}\dot{\boldsymbol{\alpha}} = \tfrac{1}{8}\begin{bmatrix}1+\eta+\zeta+\eta\zeta & 0 & 0\\ 0 & 1+\xi+\zeta+\xi\zeta & 0\\ 0 & 0 & 1+\xi+\eta+\xi\eta\end{bmatrix}\begin{bmatrix}\dot{u}\\ \dot{v}\\ \dot{w}\end{bmatrix} + \tag{33b}$$

$$\begin{bmatrix}\xi & 0 & 0\\ 0 & \eta & 0\\ 0 & 0 & \zeta\end{bmatrix}\begin{bmatrix}\dot{\alpha}_1\\ \dot{\alpha}_2\\ \dot{\alpha}_3\end{bmatrix} + \begin{bmatrix}\xi\eta & \xi\zeta & 0\\ \xi\eta & 0 & \eta\zeta\\ 0 & \xi\zeta & \eta\zeta\end{bmatrix}\begin{bmatrix}\dot{\alpha}_4\\ \dot{\alpha}_5\\ \dot{\alpha}_6\end{bmatrix}$$

The resulting element will be referred to as the EAS 6(b) element.

$$\begin{bmatrix}\dot{\varepsilon}_x\\ \dot{\varepsilon}_y\\ \dot{\varepsilon}_z\end{bmatrix} = \boldsymbol{B}\dot{\boldsymbol{u}} + \boldsymbol{M}\dot{\boldsymbol{\alpha}} = \tfrac{1}{8}\begin{bmatrix}1+\eta+\zeta+\eta\zeta & 0 & 0\\ 0 & 1+\xi+\zeta+\xi\zeta & 0\\ 0 & 0 & 1+\xi+\eta+\xi\eta\end{bmatrix}\begin{bmatrix}\dot{u}\\ \dot{v}\\ \dot{w}\end{bmatrix} + \tag{33c}$$

$$\begin{bmatrix}\xi & 0 & 0\\ 0 & \eta & 0\\ 0 & 0 & \zeta\end{bmatrix}\begin{bmatrix}\dot{\alpha}_1\\ \dot{\alpha}_2\\ \dot{\alpha}_3\end{bmatrix} + \begin{bmatrix}\xi\eta & \xi\zeta & 0 & 0 & 0 & 0\\ 0 & 0 & \xi\eta & \eta\zeta & 0 & 0\\ 0 & 0 & 0 & 0 & \xi\zeta & \eta\zeta\end{bmatrix}\begin{bmatrix}\dot{\alpha}_4\\ \dot{\alpha}_5\\ \dot{\alpha}_6\\ \dot{\alpha}_7\\ \dot{\alpha}_8\\ \dot{\alpha}_9\end{bmatrix}$$

which will be referred to as the EAS 9 element (de Borst and Groen 1995).

The favorable properties of the developed elements are demonstrated with elementary tests with the ideal plastic Drucker-Prager model on regular and distorted elements, Figure 3.

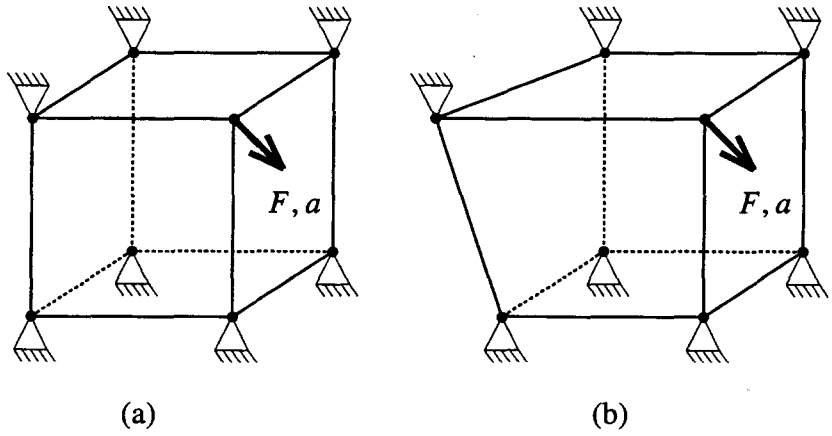

Fig. 3. Three-dimensional one-element test with roller support for volume preserving and dilatant plastic flow. (a): Rectangular element. (b): Trapezoidal element.

The adopted material parameters are a friction angle $\phi = 30°$ and a dilatancy angle $\psi = 10°$. An incremental/iterative Newton-Raphson strategy is applied to trace the equilibrium path. The computed load-displacement curves are shown in Figure 4.

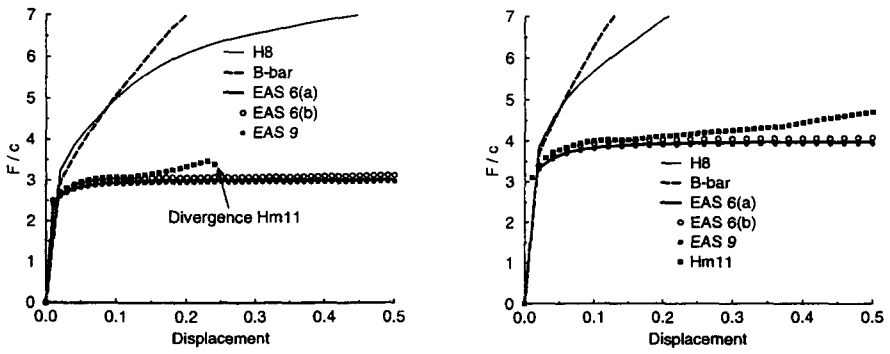

Fig. 4. Load-displacement curves for Drucker-Prager model $\psi = 10°$. (a): Rectangular element of Figure 3a. (b): Trapezoidal element of Figure 3b.

In Figure 4 we compare the standard eight-noded isoparametric brick element H8, the *B*-bar element, the modified incompatible modes element Hm11 (Taylor *et al.* 1976), and the EAS 6(a), EAS 6(b) and EAS 9 elements. It is observed that in addition to the well-known locking behavior of the standard eight-noded isoparametric brick element H8, the *B*-bar element also exhibits locking behavior which is even more pronounced. The modified incompatible modes element Hm11 also exhibits locking behavior (see also Andelfinger and Ramm 1991) and is not able to converge in the equilibrium-finding iterative procedure for the test depicted in Figure 3a, an issue that will be elaborated in the next section. All the EAS elements formulated in eq. (33) are locking free. It appears that the EAS 6(b) element gives a slightly higher yield plateau than the EAS 6(a) element.

2.4 *Stability of mixed eight-noded bricks*

Another problem that has been given less exposure in the literature than deserved is the danger that plasticity-type constitutive relations cause spurious element behavior. For this purpose we consider the element patch of Figure 5. Since the element stiffness vanishes upon ideal plastic behavior, the degree-of-freedom $\dot{\alpha}$ will be indeterminate since its value is solely dependent on the tangential compliance, even when displacement control on the degree-of-freedom "$\dot{u}$" is applied.
The forthcoming discussion is restricted to the stability of a single element. Previously, element instability has been observed by de Borst (1986) for plasticity type constitutive models and by de Borst and Rots (1989) for cracking type constitutive models. When a constitutive operator becomes singular this *should* cause a mechanism in a single finite element (otherwise the element exhibits locking behavior). However, in addition to this mechanism, some elements exhibit mechanisms which are physically unrealistic (spurious). Such spurious mechanisms will lead to either physically unacceptable solutions or to divergence of the global (equilibrium-finding) iterative procedure.

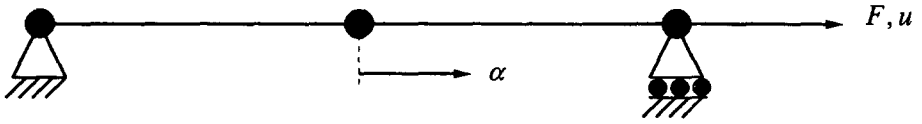

Fig. 5. A three-noded line element patch. When this patch is loaded into the ideal plastic regime, the degree-of-freedom α is indeterminate due to a vanishing stiffness.

In non-associative plastic flow without hardening, the elasto-plastic tangential matrix reads:

$$D^{ep} = D - \frac{Dmn^{T}D}{n^{T}Dm}, \tag{34}$$

in which D is the elastic stress strain relation, $n = \partial f/\partial\sigma$ is the normal to the yield surface and $m = \partial g/\partial\sigma$ is the flow direction. This matrix is singular since m is an eigenvector associated with a zero eigenvalue. This can be illustrated for the case of pure shear. In case of Von Mises or Tresca plasticity the elasto-plastic stiffness matrix D^{ep} reads:

$$D^{ep} = \frac{E}{(1+v)(1-2v)}\begin{bmatrix} 1-v & v & v & 0 \\ v & 1-v & v & 0 \\ v & v & 1-v & 0 \\ 0 & 0 & 0 & 0 \end{bmatrix} \tag{35}$$

which is singular due to a zero shear stiffness. This means that for any interpolation containing additional shear strain rates, this state of stress cannot be represented due to indeterminacy of the additional shear strain rates at the onset of plastic flow. The modified incompatible modes element Hm11 is equipped with such independent shear strain rate interpolations (Andelfinger and Ramm 1991). Hence, this element will exhibit unstable behavior which is observed from Figure 4a.
As a further illustration we will consider the case of pure tension or compression. In ideal plasticity the elasto-plastic tangential stiffness matrix has exactly one zero eigenvalue at smooth parts of the yield surface as has been shown above. This must result in one zero eigenvalue on element level for trilinear elements. Additional eigenvalues that arise at element level due to the additional strain rates will result in spurious mechanisms, which are not resisted by surrounding elements.
An eigenvalue analysis has been performed on the element stiffness matrix for the respective eight-noded brick formulations. The result is summarized in Table 1, which contains the number of zero eigenvalues of the resulting element stiffness matrix after elimination of the additional strain rate variables for an ideal plastic Mohr-Coulomb model with friction and dilatancy angles ranging from 0° to 30°.

Table 1. Number of zero eigenvalues for different eight-noded three-dimensional formulations. Pure tension Mohr-Coulomb ideal plasticity.

	H8	*B*-bar	Hm11	EAS 6(a)	EAS 6(b)	EAS 9
Regular	1	1	4	1	1	X
Distorted	1	1	1	1	1	1

It is observed from Table 1 that the spurious mechanisms caused by adding Enhanced Assumed Strain modes tend to vanish upon distortion of the element. The Hm11 element has three additional zero eigenvalues for a rectangular configuration. For the EAS 9 element condensation (31) could not even be performed. The reason is singularity of the submatrix Q, see Groen (1997).

2.5 *Footing analysis to demonstrate element properties*

The properties of the discussed eight-noded brick elements are now demonstrated via the calculation of so-called "bearing capacity factors". According to Terzaghi (1943), the limit load of a foundation can be assumed as the superposition

$$q_0 = cN_c + qN_q + \gamma\tfrac{1}{2}BN_\gamma \tag{36}$$

In which q_0 is the ultimate pressure, "c" is the cohesion, "q" is the applied pressure, γ is the soil's specific weight and "B" is the width of the foundation. N_c, N_q, N_γ are the "bearing capacity factors' for cohesion, pressure loading and weight, respectively. Here, we will focus on the bearing capacity factor for weight loading which can be expressed as

$$N_\gamma = \frac{2q_0}{B\gamma} \tag{37}$$

The applied material model is a Drucker-Prager plasticity model with a friction angle $\phi = 30°$ and a dilatancy angle $\psi = 10°$. The elastic properties of the material are Poisson's ratio $v = 0.3$ and Young's modulus $E = 10$ GPa, which should be regarded as a dummy stiffness. The coefficient of lateral earth pressure K_0 has been assumed 0.43. An incremental/iterative Newton-Raphson strategy has been applied to trace the equilibrium path. A square footing has been considered, Figure 6. The obtained load-deformation curves for the different element formulations are shown in Figure 7.
It is observed that both the *B*-bar element and the standard eight-noded trilinear isoparametric brick tend to overestimate N_γ substantially. As in the elementary test from Figure 3, the *B*-bar element results in an even higher estimation of N_γ than the standard isoparametric brick. Furthermore, it is observed that the EAS 9 element and the modified incompatible modes element Hm11 diverge in an early stage of the loading process. It appears the EAS 6(b) element performs better than the EAS 6(a) element since premature divergence was found for the latter element.

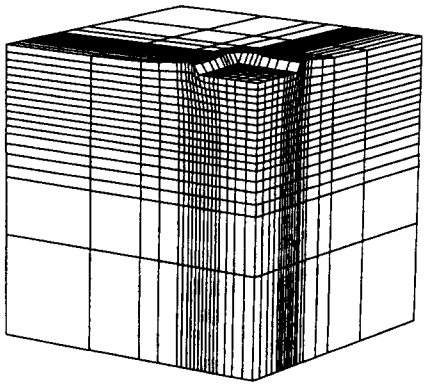

Fig. 6. Deformations

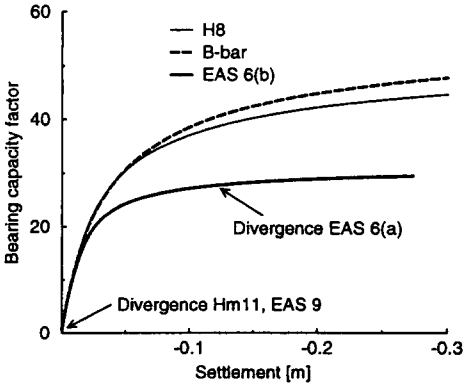

Fig. 7. Bearing capacity N_γ

3 Modeling of Clay

3.1 *Modified Cam-Clay*

The model which is discussed in this contribution belongs to the class of critical state models which originates from the work of Roscoe and his co-workers at the University of Cambridge (Roscoe and Schofield 1963, Schofield and Wroth 1968). The original idea was further developed by Roscoe and Burland (1968) to the Modified Cam-Clay model, nowadays the most widely used elasto-plastic model for the description of the mechanical behavior of clay.

The advantage of the Modified Cam-Clay model lies in its apparent simplicity and its capability to represent (at least qualitatively) the strength and deformation properties of clay realistically. Commonly observed properties such as an increasing stiffness as the material undergoes compression, hardening/softening and contractancy/dilatancy behavior, and the tendency to eventually reach a state in which the strength and volume become constant are all captured by the Modified Cam-Clay model. Moreover, calibration of the model requires only a few conventional laboratory tests.

The material description starts most conveniently with the hydrostatic components. The increasing bulk stiffness for increasing compression is modeled by

$$\dot{p} = -\frac{p}{\lambda^*}\dot{\varepsilon}_v = K_t\dot{\varepsilon}_v \qquad \text{loading} \tag{38}$$

$$\dot{p} = -\frac{p}{\kappa^*}\dot{\varepsilon}_v = K_t\dot{\varepsilon}_v \qquad \text{unloading} \tag{39}$$

λ^* and κ^* will be referred to as the "modified compression index" and the "modified swelling index", respectively (Figure 8a). As unloading is assumed to be elastic eq. (39) can be expressed using elastic components only

$$\dot{p} = -\frac{p}{\kappa}\dot{\varepsilon}_v^e = K_t\dot{\varepsilon}_v^e \tag{40}$$

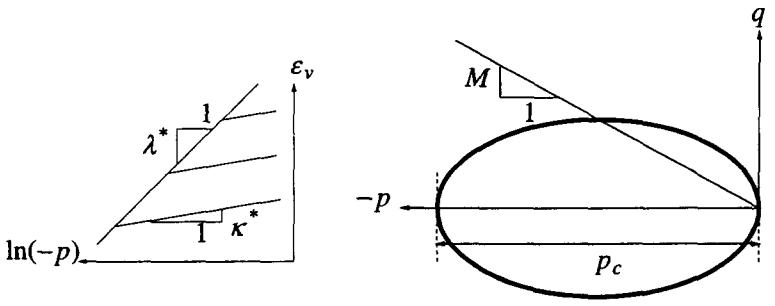

(a) (b)

Fig. 8. Material description for Modified Cam-Clay. (a): Compressive behavior. (b): Yield function and plastic potential.

For three-dimensional stress states also deviatoric components have to be specified. When eq. (40) is taken as a point of departure the assumption of isotropy, together with a constant Poisson's ratio v, gives

$$G_t = \frac{3}{2}\frac{1-2v}{1+v}K_t \tag{41}$$

The yield function is given by the expression

$$f = q^2 + M^2p(p + p_c) \tag{42}$$

in which p_c is the pre-consolidation pressure, Figure 8b. Associative plasticity is assumed so that eq. (42) also defines the plastic potential. Consequently, the plastic volumetric strain $\dot{\varepsilon}_v^p$ is given by

$$\dot{\varepsilon}_v^p = \dot{\lambda}\frac{\partial f}{\partial p} = \dot{\lambda}M^2(2p + p_c) \tag{43}$$

The deviatoric plastic strain $\dot{\gamma}^p$ is given by

$$\dot{\gamma}^p = \dot{\lambda}\frac{\partial f}{\partial \xi} = 3\dot{\lambda}R\xi \tag{44}$$

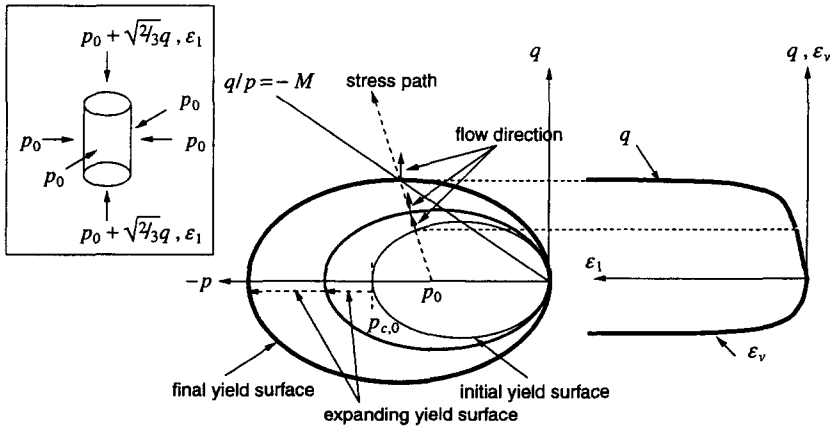

Fig. 9. Drained triaxial compression $p_{c,0} / p_0 < 2$. The associative flow rule predicts contractancy. Hence, eq. (46) predicts hardening. Eventually, monotonic loading leads to a stress ratio $q/p = -M$ where purely deviatoric ideal plastic flow is predicted.

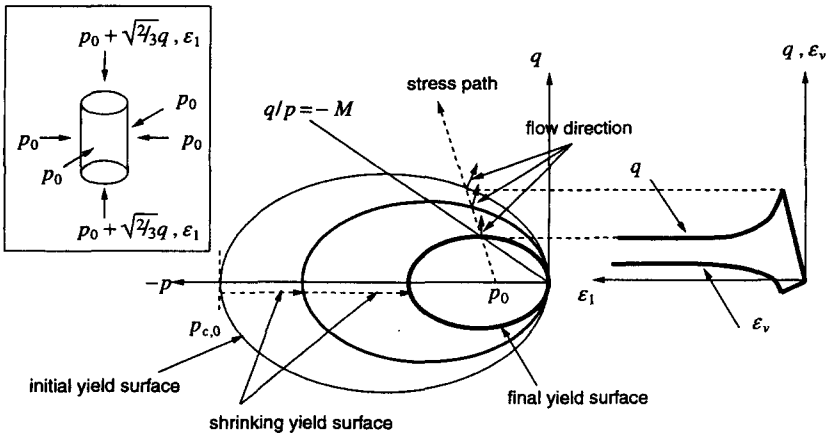

Fig. 10. Drained triaxial compression $p_{c,0} / p_0 >> 2$. The associative flow rule predicts dilatancy. Hence, eq. (46) predicts softening. Eventually, monotonic loading leads to a stress ratio $q/p = -M$ where purely deviatoric ideal plastic flow is predicted.

At this point it is convenient to define the isotropic Over-Consolidation Ratio (OCR_p) which reflects the relationship between the initial pre-consolidation pressure p_c and the current compressive pressure $-p$

$$OCR_p = \frac{p_c}{p} \tag{45}$$

Combination of definition (45) with the plastic flow direction (43) leads to the observation that when $OCR_p<2$ contractancy is predicted while when $OCR_p > 2$ dilatancy is predicted by eq. (43). Hardening/softening is determined from combination of eq. (38) and eq. (40) and the condition that during loading a stress point remains on the yield surface. This results in the following form for the evolution of p_c

$$\frac{\dot{p}_c}{p_c} = \frac{-\dot{\varepsilon}_v^p}{\lambda^* - \kappa^*} \tag{46}$$

Eq. (46) shows that contractancy leads to an increase of p_c (hardening) and dilatancy leads to a decrease p_c (softening). This behavior is most conveniently illustrated with a conventional drained triaxial compression test. The stress path in the Rendulic plane, which is representative for this test, is shown in Figure 9 and Figure 10. It is observed that when the initial value of the Over-Consolidation ratio is smaller than two ($p_{c0}/p_0 < 2$) plastic contractancy and subsequently hardening behavior is observed, Figure 9. If, on the other hand, the initial Over-Consolidation Ratio is significantly larger than two ($p_{c0}/p_0 >> 2$), plastic dilatancy and subsequently softening is predicted, Figure 10. This leads to the observation that in the Modified Cam-Clay model it is the Over-Consolidation Ratio that is responsible for the hardening/softening and contractancy/dilatancy behavior rather than the pre-consolidation pressure p_c.
Figure 9 and Figure 10 show that for constant stress paths eventually a state is reached where purely deviatoric flow is predicted. Subsequently, eq. (46) predicts ideal plastic flow. Such a state is called the critical state and is identified by $_c$

$$\frac{q}{p} = -M \tag{47}$$

The Modified Cam-Clay model is most suitable for lightly over-consolidated clays, for which the contractancy and hardening behavior are well predicted. A possible improvement which gives more accurate predictions for the coefficient of lateral earth pressure $K_0 = \sigma_h/\sigma_v$ can be found in Van Eekelen and Van den Berg (1994). For heavily over-consolidated clays, the prediction of the material behavior is less accurate (Wood 1990).
The Modified Cam-Clay model is integrated over a finite increment according to a fully implicit Euler backward algorithm (Borja 1991) including consistent tangential operators.

3.2 *Analysis of a guided pipe-jacking*

In The Netherlands, the Drinking Water Service Company of the province of South Holland has constructed a pipeline system of approximately 60 km using a guided pipe-jacking method.
The resulting surface settlements have been measured (Van den Broek *et al.* 1996). A three-dimensional analysis with the Modified Cam-Clay model is utilized for the prediction of the surface settlements.
Two top deposits have been modeled. The tunnel has a diameter of two meters and is located in the lower deposit with its center at seven meters below the surface. The interface between the upper deposit and the lower deposit is located two meters below the surface.

For the upper deposit, a compression index $\lambda^* = 0.15$ and a swelling index $\kappa^* = 0.015$ have been assumed. For the lower deposit $\lambda^* = 0.15$ and $\kappa^* = 0.03$ are adopted. Furthermore, $M = 0.877$, a density of 15 kN/m^3, an initial isotropic Over-Consolidation Ratio $OCR_{p,0} = 1.1$ and a Poisson's ratio $v = 0.2$ are adopted for both deposits. The computations have been performed with standard eight-noded isoparametric elements, ***B***-bar elements, and with the EAS 6(b) element.
Two types of analysis have been performed: (a) drained analysis in which it is assumed that the soil skeleton is completely responsible for the deformations ; (b) undrained analysis in which it is assumed that the deformations are determined by parallel action of soil and water content. Under undrained conditions the water content enforces a zero volume change upon the deformations, both in the elastic and in the plastic regime.

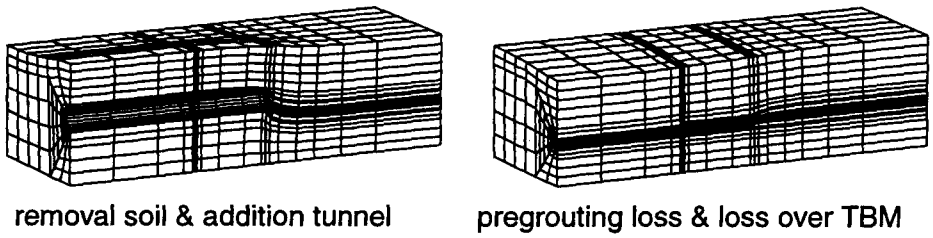

Fig. 11. Deformations at the different phases of the loading process.

The calculation has been performed in three phases:

1. (drained, one step) The gravity load is applied. It has been assumed that the tunnel lining is already present but has no weight yet. The tunnel lining has been assumed to be rigid. The weight of the soil is modeled by a point-load downwards. Moreover, it is assumed that the Tunnel Boring Machine is in-line with the tunnel lining. After the gravity load is applied, the horizontal stresses are calculated with a coefficient of lateral earth pressure $K_0 = \sigma_h/\sigma_v = 0.6$.
2. (drained/undrained, four steps) The weight of the tunnel lining is applied simultaneously with the removal of the weight of the soil in the tunnel in four steps. This has been simulated by application of a net load [WEIGHT TUNNEL LINING - WEIGHT SOIL] downwards. As the tunnel lining is lighter than the removed soil this results in an uplift of the tunnel lining and Tunnel Boring Machine.
3. (drained/undrained, twenty-five steps) Pregrouting loss around the tunnel lining is simulated by contraction of the tunnel lining which has been assumed to be ten percent of the volume of the tunnel. Loss due to the boring process is simulated by a contraction of seven percent of the volume of the tunnel around the Tunnel Boring Machine (TBM). The tunnel boring front has been supported by an overburden pressure of 0.1 bar, typical for the guided pipe-jacking method.

Not all factors that influence the deformation have been taken into account, for instance consolidation effects, the stiffness of tunnel lining and Tunnel Boring Machine and steering effects of the Tunnel Boring Machine have not been considered. However, the primary objectives of this simulation are: (a) to give at least a qualitative representation of the surface settlements; and (b) to investi-

gate the behavior of different eight-noded brick element formulations in a typical boundary value problem.

The surface settlements after the removal of soil and addition of the tunnel lining under drained conditions are displayed in Figure 12. The surface settlements resulting from the calculation with pregrouting loss and loss over the Tunnel Boring Machine under drained conditions are displayed in Figure 13.

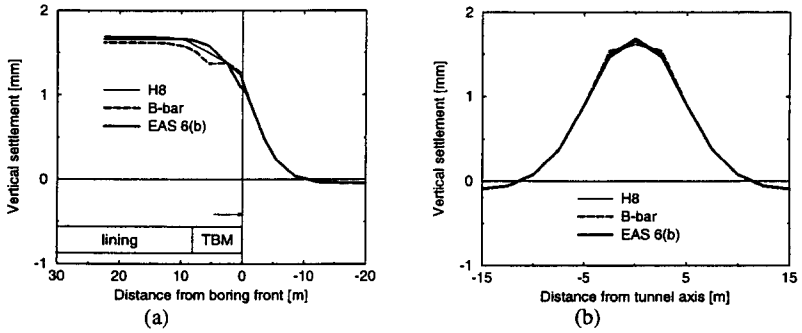

Fig. 12. Surface settlements after the removal of soil and addition of the tunnel lining for the drained analysis. (a): Settlements parallel to the tunnel. (b): Settlements 22.5 m behind the front of the Tunnel Boring Machine.

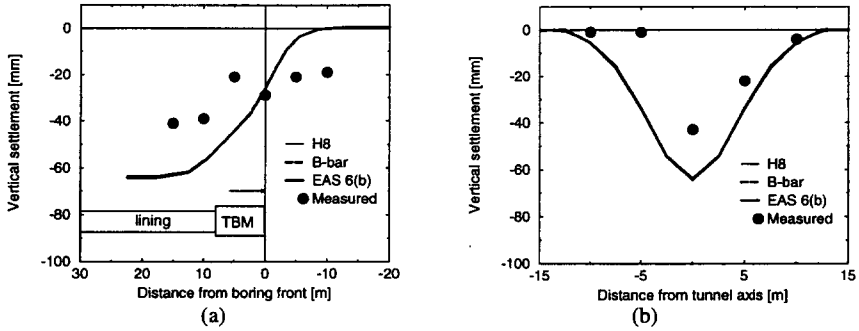

Fig. 13. Surface settlements resulting from pregrouting loss and loss over the Tunnel Boring Machine for the drained analysis. (a): Settlements parallel to the tunnel. (b): Settlements 22.5 m behind the front of the Tunnel Boring Machine.

The plastic strain distributions under drained conditions are shown in Figure 14. The surface settlements after the removal of soil and addition of the tunnel lining under undrained conditions are presented in Figure 15. The surface settlements resulting from the calculation with pregrouting loss and loss over the Tunnel Boring Machine under undrained conditions are displayed in Figure 16. The plastic strain distributions for the different element formulations under undrained conditions are shown in Figure 17.

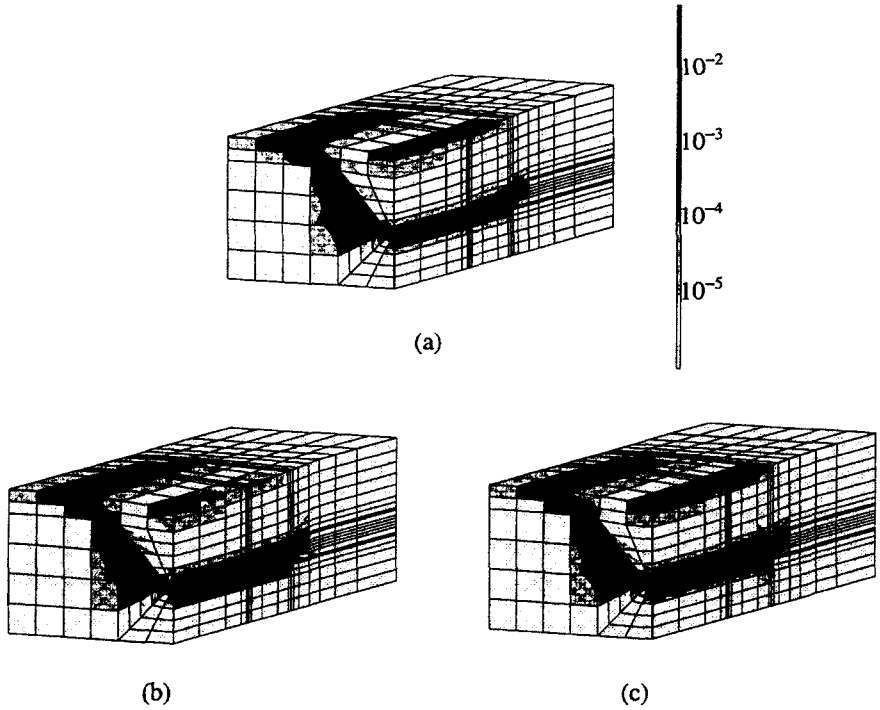

Fig. 14. Plastic strain distributions after pregrouting loss and loss around the Tunnel Boring Machine under drained conditions. (a): Standard isoparametric eight-noded brick element. (b): B-bar element. (c): EAS 6(b) element.

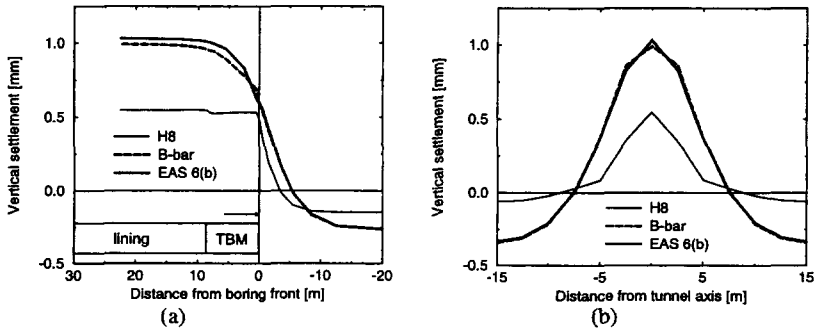

Fig. 15. Surface settlements after the removal of soil and addition of the tunnel lining for the undrained analysis. (a): Settlements parallel to the tunnel. (b): Settlements 22.5 m behind the front of the Tunnel Boring Machine.

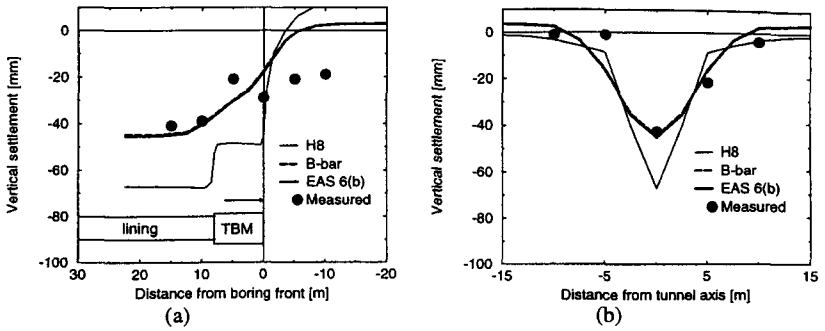

Fig. 16. Surface settlements resulting from pregrouting loss and loss over the Tunnel Boring Machine for the undrained analysis. (a): Settlements parallel to the tunnel. (b): Settlements 22.5 m behind the front of the Tunnel Boring Machine.

A comparison between Figures 12–14 (drained conditions) and Figures 15–17 (undrained conditions) shows that for drained conditions larger settlements are predicted. In case of the removal of the soil and addition of the tunnel lining (phase 2, cf. Figures 12 and 15) the smaller surface

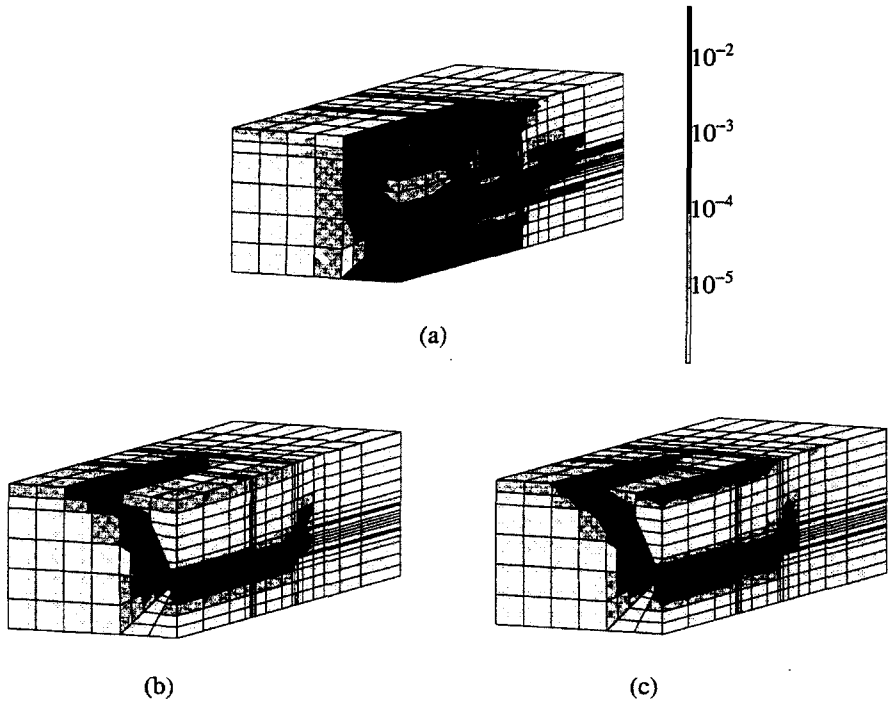

Fig. 17. Plastic strain distributions after pregrouting loss and loss around the Tunnel Boring Machine under undrained conditions. (a): Standard isoparametric eight-noded brick element. (b): B-bar element. (c): EAS 6(b) element.

settlements under undrained conditions are due to the fact that the water content acts parallel to the soil skeleton and thus leads to an increased stiffness. In case of the contraction of the tunnel lining and of the Tunnel Boring Machine (phase 3, cf. Figures 13 and 16) the smaller surface settlements under undrained conditions can be attributed to the fact that the water content enforces volume preserving deformations upon the soil skeleton. Since very lightly over-consolidated material has been assumed drained conditions result in contractancy and consequently in larger surface settlements. It can be observed from the computed surface settlements (Figures 12–13) as well as from the plastic strain distributions (Figure 14) that the different element formulations do not show significant differences under drained conditions. On the other hand, under undrained conditions severe locking behavior is observed for the standard eight-noded brick element. This becomes apparent both from the inability to represent a realistic surface settlement pattern (Figures 15–16) as well as from a severe overestimation of the plastic strains (Figure 17).

4 Modeling of sand

4.1 *A double-hardening model*

While the Modified Cam-Clay model is able to capture a large number of phenomena that occur in clayey soils with only a few parameters, it cannot describe typical phenomena that occur in sands such as simultaneous hardening and dilatancy. A possible extension would be to assume that the plastic behavior in shear is independent from the behavior in compression. This approach was first suggested by Drucker *et al.* (1957) who suggested a spherical cap on the Drucker-Prager yield surface. Later, Dimaggio and Sandler (1971), Lade (1977), Molenkamp (1980) and Vermeer (1980) followed the same approach in which, in addition to shear failure, compressive deformations were modeled by a cap. More recent models integrate the shear and compressive behavior into a single surface (Desai 1980, Kim and Lade 1988, Lade and Kim 1988a, 1988b).

In this contribution, the plastic behavior in shear and in compression will be modeled independently. This allows the formulation of a model which remains close to established concepts such as Rowe's stress-dilatancy theory (Rowe 1962) and the formulation of the compressive behavior similar to the Modified Cam-Clay model.

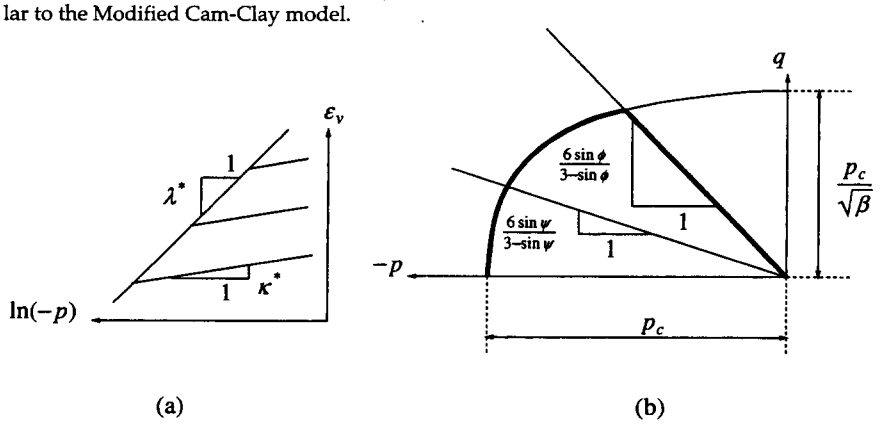

Fig. 18. Material description for the double-hardening model. (a): compressive behavior. (b): yield function and plastic potential.

As in the Modified Cam-Clay model, an increasing bulk stiffness for increasing compression is modeled by

$$\dot{p} = -\frac{p}{\lambda^*}\dot{\varepsilon}_v = K_t\dot{\varepsilon}_v \qquad \text{loading} \tag{48}$$

$$\dot{p} = -\frac{p}{\kappa^*}\dot{\varepsilon}_v = K_t\dot{\varepsilon}_v \qquad \text{unloading} \tag{49}$$

with λ^* the "modified compression index" and κ^* the "modified swelling index" (Figure 18a). As unloading is assumed to be elastic eq. (49) can be expressed using elastic components only

$$\dot{p} = -\frac{p}{\kappa^*}\dot{\varepsilon}_v^e = K_t\dot{\varepsilon}_v^e \tag{50}$$

When eq. (50) is taken as a point of departure, the assumption of isotropy, together with a constant Poisson's ratio v, gives the following expression for the tangent shear modulus G_t

$$G_t = \frac{3}{2}\frac{1-2v}{1+v}K_t \tag{51}$$

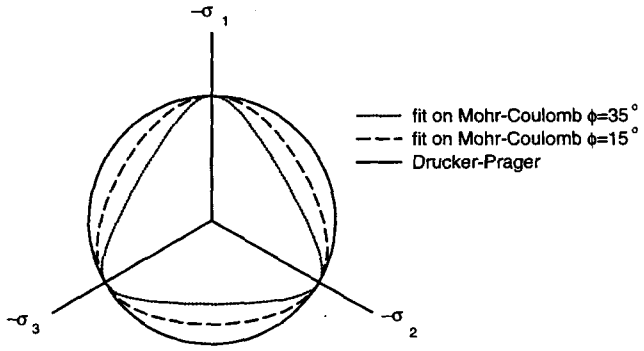

Fig. 19. Yield function (52) in the deviatoric plane.

Shear failure is assumed to occur on a Drucker-Prager type failure surface

$$f_1 = \left(\frac{1-\alpha\cos 3\theta}{1-\alpha}\right)^{-n} q + \frac{6\sin\phi}{3-\sin\phi}\,p \tag{52}$$

in which ϕ is the friction angle, and α and n are parameters which include the effect of the Lode angle ϕ. A projection of the yield function (52) in the deviatoric plane is shown in Figure 19. Optimal properties regarding convexity are obtained when $n = -0.229$ (Van Eekelen 1980). Convexity is then retained for $\alpha \leq 0.7925$, which corresponds to a fit through all the corners of the Mohr-Coulomb criterion for a friction angle of 46.55°. Pastic flow on the shear failure surface (52) is assumed to be non-associative and is determined by the Drucker-Prager plastic potential

$$g_1 = q + \frac{6\sin\psi}{3-\sin\psi}p \tag{53}$$

in which ψ is the dilatancy angle. This assumption of a Drucker-Prager plastic potential is motivated by experimental results from Kim and Lade (1988) which indicate a plastic potential close to a Drucker-Prager contour in the deviatoric plane.
During compaction, plastic straining is described by the compression cap

$$f_2 = p^2 + \beta q^2 - p_c^2 \tag{54}$$

where associative plasticity is assumed. In eq. (54), β is a shape parameter which is used to fit the prediction of the coefficient of lateral earth pressure $K_0 = \sigma_h / \sigma_v$ (Van Langen 1991). p_c is a measure for the current degree of over-consolidation and can be determined from an isotropic Over-Consolidation Ratio (OCR_p) similar to the Modified Cam-Clay model

$$OCR_p = \frac{p_c}{p} \tag{55}$$

or alternatively, from an Over-Consolidation Ratio (OCR) which is based on the size of the cap (54) and thus includes the effect of the effective deviatoric stress

$$OCR_p = \frac{p_c}{\sqrt{p^2 + \beta q^2}} \tag{56}$$

The plastic strain rates are assumed to be an additive decomposition of plastic strain rates $\boldsymbol{\varepsilon}_1^p$ on the shear failure surface (52) and plastic rates $\boldsymbol{\varepsilon}_2^p$ on the compression cap (54)

$$\dot{\boldsymbol{\varepsilon}}^p = \dot{\boldsymbol{\varepsilon}}_1^p + \dot{\boldsymbol{\varepsilon}}_2^p \tag{57}$$

This leads to the following expression for the volumetric plastic strain rates

$$\dot{\varepsilon}_v^p = \dot{\lambda}_1 \frac{\partial g_1}{\partial p} + \dot{\lambda}_2 \frac{\partial f_2}{\partial p} = \dot{\lambda}_1 \frac{6\sin\psi}{3-\sin\psi} + 2p\dot{\lambda}_2 \tag{58}$$

and for the deviatoric plastic strain rates

$$\dot{\gamma}^p = \dot{\lambda}_1 \frac{\partial g_1}{\partial \boldsymbol{\xi}} + \dot{\lambda}_2 \frac{\partial f_2}{\partial \boldsymbol{\xi}} = \dot{\lambda}_1 \tfrac{3}{2} \frac{\boldsymbol{R}\boldsymbol{\xi}}{q} + \dot{\lambda}_2 3\boldsymbol{R}\boldsymbol{\xi} \tag{59}$$

Friction hardening is assumed according to

$$\sin\phi = \sin\phi(\gamma^p_{eff}) \tag{60}$$

in which γ^{p}_{eff} is defined as the effective deviatoric plastic strain on the failure surface (Vermeer 1980) which is defined in a rate form

$$\dot{\gamma}^{p}_{eff} = \sqrt{\frac{2}{3}\dot{\gamma}^{p_T}_{1} R^{-1} \dot{\gamma}^{p}_{1}} \tag{61}$$

Eq. (61) leads to a convenient relationship between the rate of the plastic multiplier on the failure surface $\dot{\lambda}_1$ and $\dot{\gamma}^{p}_{eff}$

$$\dot{\gamma}^{p}_{eff} = \dot{\lambda}_1 \tag{62}$$

Dilatancy is assumed to obey Rowe's stress-dilatancy theory in triaxial compression

$$\sin\psi = \frac{\sin\phi - \sin\phi_{cv}}{1 - \sin\phi\sin\phi_{cv}} \tag{63}$$

in which ϕ_{cv} is identified as the so-called "friction angle at constant volume (Vermeer and de Borst 1984). The evolution of hardening on the cap (54) is derived from the loading function (48), eq. (50) and the condition that during compressive loading a stress point is located on the cap (46). This results in the following form for the evolution of p_c

$$\frac{\dot{p}_c}{p_c} = \frac{-\dot{\varepsilon}^{p}_{v,2}}{\dot{\lambda} - \dot{\kappa}} \tag{64}$$

in which $\dot{\varepsilon}^{p}_{v,2}$ is the plastic volumetric strain rate on the cap.
The Modified Cam-Clay model is integrated over a finite increment according to a fully implicit Euler backward algorithm (Borja 1991) which has been extended to three stress invariants (Groen 1997). The algorithm is amenable to exact linearization, which enables the derivation of a consistent tangential operator.

4.2 *Analysis of the leaning tower of Pisa*

The leaning tower of Pisa is a challenging problem in geomechanics. A three-dimensional numerical simulation has been carried out in order to investigate the effect of the lead blocks that have been applied on the high-side of the tower in 1993 in order to reduce the inclination.
It is not the objective of this calculation to give a quantitative representation of the deformations under the tower. The geotechnical conditions as well as the loading conditions on the foundation of the tower are simply too complicated. Moreover, the uncertainty in the constitutive parameters is too large to give any realistic prediction of the true deformations that occur in the subsoil under the tower. However, the three-dimensional character as well as the relatively clear classification of the constitutive parameters makes the leaning tower of Pisa an excellent benchmark for assessment of the performance of the adopted double-hardening model as well as for the performance of the Enhanced Assumed Strain elements.
Calabresi *et al.* (1993) have performed triaxial tests on the soil deposits underneath the tower and have proposed Modified Cam-Clay parameters for the clayey deposits and Mohr-Coulomb frictional parameters for the sandy deposits. The material parameters proposed by Calabresi *et al.* (1993) are adapted to the double-hardening model, Table 2.

It is assumed that the respective friction angles do not change during the loading process. The parameter α is adjusted such that a fit through all the corners of the Mohr-Coulomb yield function is obtained for each deposit. Furthermore, a dilatancy angle $\psi = 0$ and a Poisson's ratio $v = 0.12$ are assumed for all deposits.
The foundation of the tower is assumed to have a density $\rho = 21.43\ [kN/m^3]$, a Young's modulus of $E = 1.5 \times 10^6\ [\ kPa\ ]$, a Poisson's ratio $v = 0.12$ and a coefficient of lateral earth pressure $K_0 = 0.92$. Alternatively, a set of material properties has been used with a linear elastic approximation for the compressive behavior (Grashuis 1993), Table 3.

Table 2. Material properties for the respective deposits under the tower. The material parameters proposed by Calabresi *et al.* (1993) are adapted to the double-hardening model.

depth [m]	E *[kPa]*	κ^*	λ^*	$\sin(\phi)$	OCR	K_0	$\rho\ [kN/m^3]$
0–1.4	–	0.00486	0.0481	0.555	4.2	0.92	21.43
1.4–5.4	–	0.00495	0.049	0.554	3.0	0.79	19.17
5.4–7.4	$1{,}25\times10^4$	–	–	0.559	–	0.45	15.40
7.4–17.8	–	0.014	0.107	0.446	1.35	0.69	18.49
17.8–22	–	0.0151	0.0722	0.479	1.8	0.67	19.64
22–24.4	1.8×10^4	–	–	0.564	–	0.43	20.40
24.4–37	–	0.0106	0.0851	0.424	1.1	0.56	21.66

Table 3. Material properties for the respective deposits under the tower. The compressive indices in Calabresi *et al.* (1993) are approximated by a linear elastic compressive stiffness based on the initial stress state (Grashuis 1993).

depth [m]	E *[kPa]*	$\sin(\phi)$	K_0	$\rho\ [kN/m^3]$
0–1.4	3×10^3	0.555	0.92	21.43
1.4–5.4	3×10^3	0.554	0.79	19.17
5.4–7.4	1.25×10^4	0.559	0.45	15.40
7.4–17.8	8×10^3	0.446	0.69	18.49
17.8–22	1.4×10^4	0.479	0.67	19.64
22–24.4	1.8×10^4	0.564	0.43	20.40
24.4–37	2.5×10^4	0.424	0.56	21.66

Three different formulations for the eight-noded brick element are compared: the standard isoparametric element H8, the *B*-bar element and the EAS 6(a) element.
The vertical stress state under the tower is initialized with the self-weight of the soil skeleton. The horizontal stresses are then calculated with the coefficient of lateral earth pressure $K_0 = \sigma_h/\sigma_v$. Drained conditions have been assumed (i.e. no influence of the ground water on the deformation behavior). The loading history is simulated by three phases:

1. The weight of the tower is applied in twenty-nine steps under drained conditions.
2. The moment on the foundation due to the inclination of the tower is applied in twenty steps under drained conditions.
3. The weight and the moment due to the lead-blocks are applied in eight steps. Both drained conditions and undrained conditions are simulated.

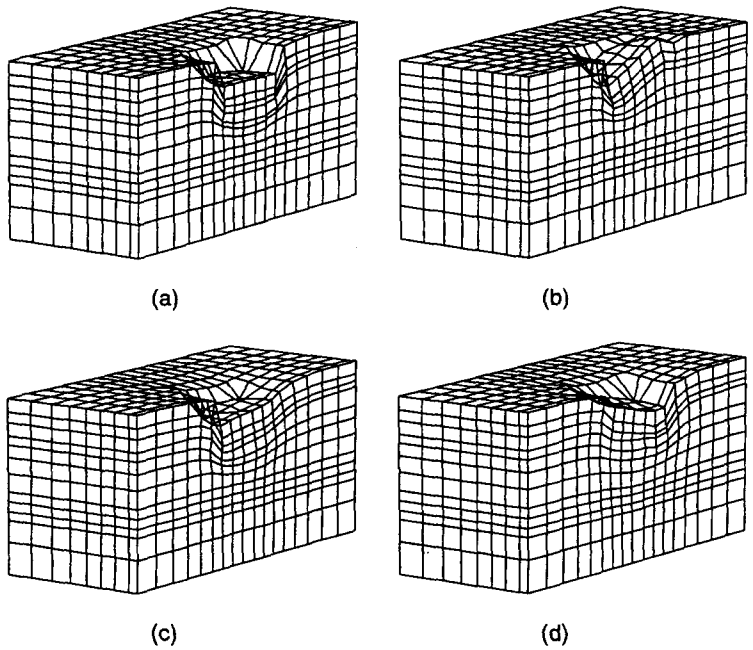

Fig. 20. Incremental deformations for the material properties listed in Table 2. (a): After application of the weight of the tower. (b): After application of the moment due to the inclination of the tower. (c): After application of the lead-blocks on the high side of the tower under drained conditions. (d): After application of the lead-blocks on the high side of the tower under undrained conditions.

Figure 20 shows the incremental deformations as a result of the loading history for the material properties listed in Table 2. A salient feature of these material properties is that the application of the lead blocks under drained conditions tends to increase the inclination of the tower, Figure 20c. Figure 21 shows the applied moment versus the inclination of the tower. It is observed that the material parameters listed in Table 2 give an inclination of approximately 1.2° while the simulation with the material parameters listed in Table 3 gives a much softer response (an inclination of

approximately 3.5°). It is also observed that the different formulations for the eight-noded brick element do not show spectacular differences.

Figure 22 shows the Von Mises stress distributions after application of the lead blocks for the different eight-noded brick element formulations under drained conditions for the material properties listed in Table 2. Figure 23 shows the Von Mises stress distributions after application of the lead blocks for the different eight-noded brick element formulations under undrained conditions for the material properties listed in Table 3.

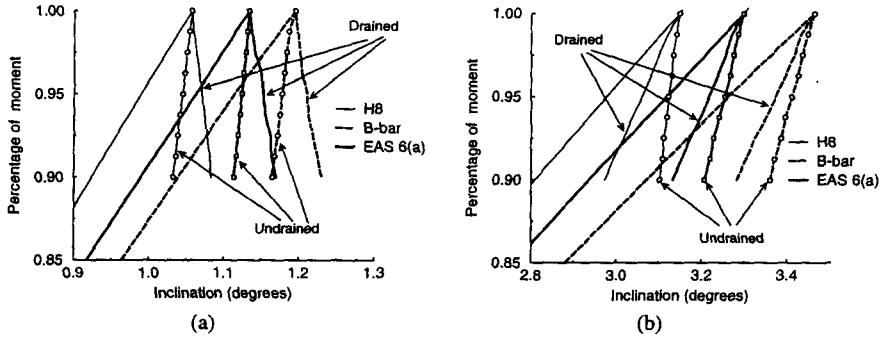

Fig. 21. Moment versus inclination of the tower. (a): Utilizing the material parameters from Table 2. (b): Utilizing the material parameters from Table 3.

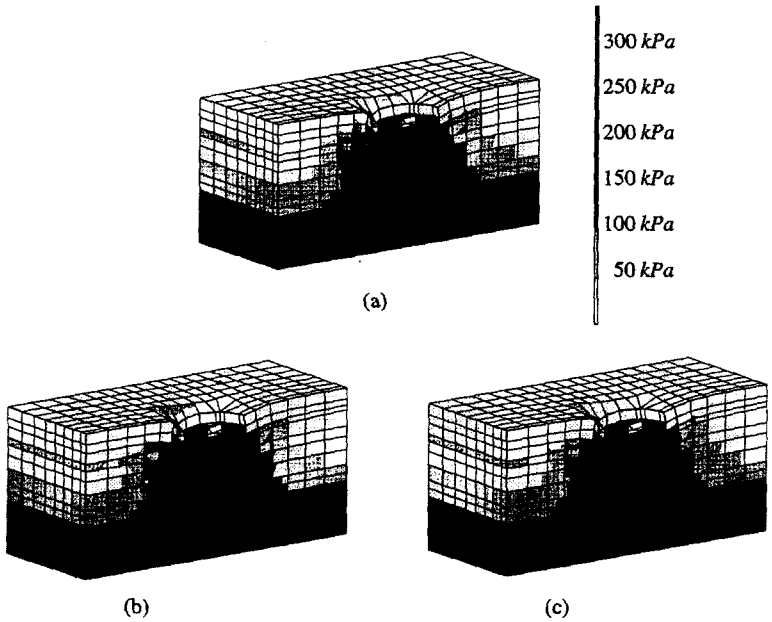

Fig. 22. Von Mises stress distributions after application of the lead blocks under drained conditions with the material properties from Table 2. (a): standard isoparametric element. (b): B-bar element. (c): EAS 6(a) element.

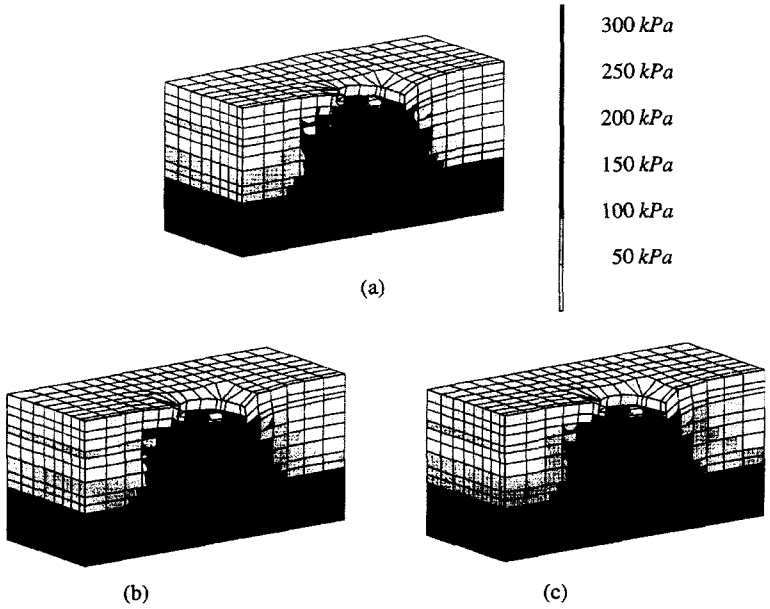

Fig. 23. Von Mises stress distributions after application of the lead blocks under undrained conditions with the material properties from Table 2. (a): standard isoparametric element. (b): B-bar element. (c): EAS 6(a) element.

It is observed from Figure 22 and Figure 23 that the stress patterns obtained with the different element types do not show spectacular differences. However, the stress patterns obtained with the standard isoparametric element are somewhat oscillatory compared to the other element types, especially in the undrained case.

5 Conclusions

The performance of low-order elements has been scrutinized in volume preserving and dilatant plastic flow. The Enhanced Assumed Strain concept (Simo and Rifai 1990) has been adopted in order to remedy the characteristic locking behavior. Elementary tests as well as a realistic boundary value problem indicate the favorable properties of the proposed eight-noded bricks. All the analytical considerations have been performed under the assumption of a Mohr-Coulomb plasticity model in which the principal stress / strain axes coincide with the isoparametric axes. However, it has been demonstrated that volumetric locking can also be avoided for trapezoidal element shapes and for a realistic boundary value problem. Also, it has been observed that the *B*-bar element, after a initially weaker response, can exhibit an even stiffer response than the standard eight-noded isoparametric brick in dilatant plastic flow.

The Modified Cam-Clay model has been presented. An analysis of a guided pipe-jacking has been performed to assess the performance of different eight-noded brick elements in combination with the Modified Cam-Clay model under drained and undrained conditions. It has been observed that the different element formulations do not give significant differences for this problem under drained conditions. However, under undrained conditions the standard eight-noded isoparametric brick element revealed pronounced locking behavior which followed from the observation of unrealistic deformation patterns as well as from a significant overestimation of the plastic strains.
A double-hardening model has been presented for the behavior of sand including non-linear elastic behavior similar to the Modified Cam-Clay model. The leaning tower of Pisa has been used as a benchmark to assess the performance of the double-hardening model. A comparison between different eight-noded brick element formulations has been given for this benchmark. An interesting observation is that the parameters adopted here in combination with drained behavior yielded a further inclination of the tower as a result of the application of the lead blocks.
Both the simulation of the guided pipe-jacking and of the leaning tower of Pisa were performed in a reasonable number of steps (30–60) with a Newton-Raphson iterative scheme. This underlines the applicability and performance of modern computational techniques such as described in Borja (1991) to three-dimensional geotechnical applications. Also, from both simulations it has been observed that the differences between the element formulations are minor in drained analysis. From this it can be concluded that the difference between the element formulations only becomes significant when the influence of the deformation constraint becomes sufficiently large. This is for instance the case in undrained analysis where volume preserving conditions are present throughout the computation or during calculation of collapse loads as has been exemplified by the determination of bearing capacities of the square footing.

Acknowledgements

Financial support of the Dutch Technology Foundation under grant DCT22.2930 and from the Center for Civil Engineering Research, Codes and Specifications is gratefully acknowledged.

References

Andelfinger, U. and Ramm, E. (1991), EAS-elements for 2D, 3D, plate and shell structures and their equivalence to HR elements. *Int. J. Num. Meth. Engng.*, Vol. 36, pp. 1311–1337.

Borja, R., (1991), Cam-clay plasticity, Part II, Implicit integration of constitutive equations based on a nonlinear elastic stress predictor. *Comp. Meth. Appl. Mech. Engng.*, Vol. 88, pp. 225–240.

Van Den Bogert, P.A.J., De Borst, R., Luiten, G.T. and Zeilmaker, J. (1991), Robust finite elements for 3D analysis of rubber-like materials. *Engng. Comp.*, Vol. 8, pp. 3–17.

Calabresi, G., Rampello, S. and Callisto, L. (1993), The leaning tower of Pisa, geotechnical characterisation of the tower's subsoil within the framework of the critical state theory. *Studie Recherche, Universita degli Roma "La Sapienza"*

De Borst, R. (1982), Calculation of collapse loads using higher order elements. IUTAM *Symposium on Deformation and Failure of Granular Materials.* Balkema, Rotterdam, pp. 503-513.

De Borst, R. (1986), *Non-linear analysis of frictional materials.* Dissertation, Delft University of Technology.

De Borst, R. and Rots, J.G. (1989), Occurrence of spurious mechanisms in computations of strain-softening solids. *Engng. Comput.*, Vol. 6, pp. 272–280.

De Borst, R. and Groen, A.E., (1995), Some observations on element performance in isochoric and dilatant plastic flow. *Int. J. Num. Meth. Engng.*, Vol. 38, pp. 2887–2906.

Desai, C.S., (1980), A general basis for yield, failure and potential functions in plasticity. *Int. J. Num. Anal. Meth. Geom.*, Vol. 4, pp. 361–375.

Dimaggio, F.L., and Sandler, I.V., (1971), Material model for granular soils. *J. Engng. Mech. Div. ASCE*, 97, pp. 935–950.

Drucker, D.C., Gibson, R.E. and Henkel, D.J. (1957), Soil mechanics and work hardening theories of plasticity. *Trans.* ASCE, 122 pp. 338–346.

Grashuis, A.J. (1993), Pisa-Toren berekening en validatie Pluto-3D *Report SE-57013*, Delft Geotechnics.

Groen, A.E. (1997), *Three-dimensional elasto-plastic analysis of soils.* Dissertation, Delft University of Technology.

Hughes, T.J.R. (1980), Generalization of selective integration procedures to anisotropic and non-linear media. *Int. J. Num. Meth. Engng.* Vol. 15, pp. 1413-1418.

Hughes, T.J.R. (1987), *The Finite Element Method.* Prentice-Hall, Englewood cliffs, New Jersey.

Kim, M.K., and Lade, P.V. (1988), Single hardening constitutive model for frictional materials I. Plastic potential function. *Computers and Geotechnics*, Vol 5, pp. 307–324.

Lade, P.V. (1977), Elasto-plastic stress-strain theory for cohesionless soil with curved yield surfaces, *Int. J. Sol. Struct.*, Vol. 13, pp. 1019-1035.

Lade, P.V. and Kim, M.K. (1988a), Single hardening constitutive model for frictional materials II. Yield criterion and plastic work contours. *Computers and Geotechnics*, Vol. 6, pp. 13–29.

Lade, P.V. and Kim, M.K. (1988b), Single hardening constitutive model for frictional materials III. Comparisons with experimental data. *Computers and Geotechnics* Vol. 6, pp. 31–47.

Molenkamp, F. (1980), Elasto-plastic double hardening model MONOT. *LGM Report CO-218595*, Delft Geotechnics.

Nagtegaal, J.C., Parks, D.M. and Rice, J.R. (1974), On numerically accurate finite element solutions in the fully plastic range *Comp. Meth. Appl. Mech. Engng.*, Vol. 4, pp. 153–177.

Roscoe, K.H. and Schofield, A.N. (1963), Mechanical behaviour of an idealised "wet" clay. In: *Proc. European Conf. on Soil Mechanics and Foundation Engineering, Wiesbaden*, Vol. 1, pp. 47–54.

Roscoe, K.H. and Burland, J.B., (1968), On the generalized behaviour of "wet" clay. In: *Engineering plasticity*. 48: pp. 535–609, Cambridge University Press, Cambridge.

Rowe, P.W., (1962), The stress-dilatancy relation for static equilibrium of an assembly of particles in contact. *Proc. Roy. Soc. London.* A269: pp. 500–527.

Schofield, A.N. and Wroth, C.P. (1968), *Critical state soil mechanics,* McGraw Hill, London.

Simo, J.C. and Rifai, M.S. (1990), A class of mixed assumed strain methods and the method of incompatible modes. *Int. J. Num. Meth. Engng.*, Vol. 29, pp. 1595–1638.

SLOAN, S.W. and RANDOLPH, M.F. (1982), Numerical prediction of collapse loads using finite element methods. *Int. J. Num. Anal. Meth. Geom.*, Vol. 6, pp. 47–76.

SUSSMAN, T. and BATHE, K.J. (1987), A finite element formulation for nonlinear incompressible elastic and inelastic analysis. *Comp. Struct.*, Vol. 29, pp. 357–409.

TAYLOR, R.L., BERESFORD, P.J. and WILSON, E.L. (1976), A non-conforming element for stress analysis. *Int. J. Num. Meth. Engng.*, Vol. 10, pp. 1211–1219.

TAYLOR, R.L., SIMO, J.C., ZIENKIEWICZ, O.C. and CHAN, C.H. (1986), The patch test - A condition for assessing FEM convergence. *Int. J. Num. Meth. Engng.*, Vol. 22, pp. 39–62.

TERZAGHI, K. (1943), *Theoretical Soil Mechanics*. Wiley, New York.

VAN DEN BROEK, W.L.A.H., DE BORST, R. and GROEN, A.E. (1996), Two- and Three-dimensional modelling of a guided pipe-jacking in soft soil. *Geotechnical Aspects of Underground Construction in Soft Ground*. Balkema, Rotterdam. pp. 419–422.

VAN EEKELEN, H.A.M. (1980). Isotropic yield surfaces in three dimensions for use in soil mechanics. *Int. J. Num. Anal. Meth. Geom.*, Vol. 4, pp. 89-101.

VAN EEKELEN, S.J.M. and VAN DEN BERG, P. (1994), The Delft egg model, a constitutive model for clay. In: *DIANA Computational Mechanics '94*, Kusters, G.M.A. and Hendriks, M.A.N. (eds), pp. 103–116, Kluwer Academic Publishers, Dordrecht.

VAN LANGEN, H. (1991), *Numerical analysis of soil-structure interaction*. Dissertation, Delft University of Technology.

VERMEER, P.A. (1980), *Formulation and analysis of sand deformation problems*. Dissertation, Delft University of Technology.

VERMEER, P.A. and DE BORST, R. (1984), Non-associated plasticity for soils, concrete and rock. *Heron* Vol. 29(3), pp. 1–64.

WILSON, E.L., TAYLOR, R.L., DOHERTY, W.P. and GHABOUSSI, J. (1971), Incompatible displacement models, in S.J. Fenves *et al. Numerical and Computer Models in Structural analysis, Academic press, New York.*

WOOD, D.M. (1990), *Soil behaviour and critical state soil mechanics*. Cambridge University Press, Cambridge.

ZIENKIEWICZ, O.C. and TAYLOR, R.L. (1989), *The finite element method, 4th ed.* McGraw-Hill.